Energy & Environmental Science

PAPER

View Article Online
View Journal | View Issue

Cite this: *Energy Environ. Sci.*, 2016, **9**, 530

New insight into the material parameter *B* to understand the enhanced thermoelectric performance of $Mg_2Sn_{1-x-y}Ge_xSb_y$†

Weishu Liu,[a] Jiawei Zhou,[b] Qing Jie,[a] Yang Li,[c] Hee Seok Kim,[a] Jiming Bao,[c] Gang Chen*[b] and Zhifeng Ren*[a]

Received 22nd August 2015,
Accepted 12th November 2015

DOI: 10.1039/c5ee02600h

www.rsc.org/ees

Historically, a material parameter *B* incorporating weighted mobility and lattice thermal conductivity has guided the exploration of novel thermoelectric materials. However, the conventional definition of *B* neglects the bipolar effect which can dramatically change the thermoelectric energy conversion efficiency at high temperatures. In this paper, a generalized material parameter *B** is derived, which connects weighted mobility, lattice thermal conductivity, and the band gap. Based on the new parameter *B**, we explain the successful tuning of the electron and phonon transport in $Mg_2Sn_{1-x-y}Ge_xSb_y$, with an improved *ZT* value from 0.6 in $Mg_2Sn_{0.99}Sb_{0.01}$ to 1.4 in $Mg_2Sn_{0.73}Ge_{0.25}Sb_{0.02}$. We uncover that the Ge alloying approach simultaneously improves all the key variables in the material parameter *B**, with an ~25% enhancement in the weighted mobility, ~27% band gap widening, and ~50% reduction in the lattice thermal conductivity. We show that a higher generalized parameter *B** leads to a higher optimized *ZT* in $Mg_2Sn_{0.73}Ge_{0.25}Sb_{0.02}$, and some common thermoelectric materials. The new parameter *B** provides a better characterization of material's thermoelectric transport, particularly at high temperatures, and therefore can facilitate the search for good thermoelectric materials.

Broader context

Thermoelectric conversion involves the transport of electrons and phonons. It has been very challenging to synergistically tune the macro thermoelectric transport parameters: electrical conductivity, thermal conductivity, and Seebeck coefficient as these properties are coupled to each other. Recently, we have achieved a significant enhancement in the thermoelectric performance of Mg_2Sn by partially substituting Sn with Ge and doping Sb as donor. The new material $Mg_2Sn_{0.728}Ge_{0.25}Sb_{0.022}$ has a high average *ZT* (0.9) and a power factor (52 μW cm^{-1} K^{-2}) in the temperature range of 25–450 °C, with favourably high efficiency and large output power density. The *ZT* improvement is understood through a generalized material parameter *B**, which connects weighted mobility, lattice thermal conductivity, and the band gap. A higher *B** is desired for higher *ZT*. The new parameter will help guide the optimizations of known materials by synergistically tailoring these fundamental parameters to enhance their thermoelectric performance, and the search for new materials.

1. Introduction

The efficiency of thermoelectric power generation is governed by the Carnot efficiency and dimensionless figure of merit (*ZT*) of the material. *ZT* is defined as $ZT = (S^2\sigma/\kappa)T$, where *S*, σ, κ, and *T* are the Seebeck coefficient, electrical conductivity, thermal conductivity, and absolute temperature, respectively.[1] The *ZT* value strongly depends on the carrier concentration. Optimization of the carrier concentration leads to optimized reduced Fermi energy ($\xi_f = E_f/k_BT$) close to the band edge E_c for n-type and E_v for the p-type semiconductor,[2] where the energy is measured from E_c (E_v) for the n-type (p-type) semiconductor. However, the maximum *ZT* is limited by the interdependence of *S*, σ, and κ.[3] In evaluating material's thermoelectric performance, a dimensionless material parameter *B*, proposed first by Chasmar and Stratton from a single parabolic band model in the nondegenerate limit, has proven to be very useful.[4–8]

$$B = 5.745 \times 10^{-6} \frac{\mu (m^*/m_0)^{3/2}}{\kappa_{lat}} T^{5/2}, \quad (1)$$

[a] Department of Physics and TcSUH, University of Houston, Houston, Texas 77204, USA. E-mail: zren@uh.edu; Fax: +1-713-743-8201; Tel: +1-713-743-8227
[b] Department of Mechanical Engineering, Massachusetts Institute of Technology, Cambridge, Massachusetts 02139, USA. E-mail: gchen2@mit.edu; Fax: +1-617-324-5519; Tel: +1-617-253-0006
[c] Department of Electrical and Computer Engineering, University of Houston, Houston, Texas 77204, USA

† Electronic supplementary information (ESI) available. See DOI: 10.1039/c5ee02600h

where m^*, m_0, μ, κ_{lat}, and T are the carrier effective mass, free electron mass, carrier mobility, lattice thermal conductivity, and absolute temperature, respectively. All the parameters defined in eqn (1) are expressed in SI units, *i.e.*, μ in $m^2\ V^{-1}\ s^{-1}$ and κ_{lat} in $W\ m^{-1}\ K^{-1}$. The product of μ and $(m^*/m_0)^{3/2}$ was commonly called weighted mobility and will be denoted as U. A large material parameter B usually corresponds to a high ZT value at the optimized ξ_f. The power of this parameter lies in the fact that it provides a clear guidance to identify better thermoelectric materials instead of checking all the transport properties (S, σ, and κ); one should look for materials with a high weighted mobility U and low lattice thermal conductivity κ_{lat}, which are less dependent on each other. Furthermore, the material parameter B was generalized to take into account the effect of alloying scattering,[9] as well as additional electron (hole) bands.[10] Despite the insightful understandings gained from the parameter B, eqn (1) implies that this parameter increases with the temperature continuously, while ZT of the most real materials drops at high temperatures due to the bipolar effect. It has been known that materials with a small energy band gap (E_g) suffer more from the bipolar effect due to the decreased Seebeck coefficient and increased thermal conductivity.[11] Previous work has shown that the optimized band gap is related to the temperature, *i.e.*, $E_g = (4\text{–}10)k_BT$.[4,12,13] For given material parameter B and temperature T, the optimized ZT with respect to the carrier concentration increases with the band gap and becomes saturated as $E_g > 10k_BT$ for both direct and indirect band gaps.[13,14] However, a generalized material parameter similar to B is missing that permits the evaluation of material's thermoelectric performance by exploring the tradeoff among U, κ_{lat}, and E_g in a more fundamental way rather than examining S, σ, and κ.

The nanoapproach has worked for most of the thermoelectric materials because the scattering centers scatter phonons more than electrons.[15,16] Recently, a first-principles-based simulations for silicon have shown that the length span of the mean free path of phonons is much longer than that of electrons, which give a good explanation for enhanced ZT from the nanoapproach strategy.[17] However, further reduction of κ_{lat} may lead to reduced U, when the average distance between two neighbor scattering centers becomes comparable to the electron mean free path. Different strategies have been developed to reduce the decrease of the carrier mobility when applying the nanostructuring approach to reduce κ_{lat}, such as modulation doping,[18] ordered nanoinclusion,[3] re-oriented grains,[19] and better alignment of band edge offsets between the inclusions and the matrix.[20] In another direction different from the phonon engineering, increased electronic density-of-states due to resonant dopants,[21–23] and the band convergence effect[24,25] has been used to improve the power factor by increasing the effective mass. Furthermore, there is one constraint between E_g and κ_{lat}. For two compounds with similar crystalline structures, the one composed of lighter elements usually has larger E_g and higher κ_{lat} due to stronger chemical bonding.[26] One way to go beyond this limit is to have a complex crystalline structure as complex crystal structures have more optical phonons that do not contribute much to heat conduction and yet can scatter acoustic phonons, leading to a lower lattice thermal conductivity.[27] Despite various strategies mentioned above, there does not exist a unified parameter connecting the three fundamental parameters U, κ_{lat}, and E_g to guide the improvement of ZT.

In this work, we derive a generalized material parameter B^*, which is proportional to U and E_g while inversely proportional to κ_{lat}, and apply it to understand the enhanced thermoelectric performance of alloyed Mg_2Sn. Mg_2Sn is a semiconductor with a narrow band gap of 0.26 eV,[28] which has recently been investigated in the composition of $Mg_2Sn_{0.6}Si_{0.4}$, showing a ZT of 1.1–1.3.[29–34] In our previous work,[35] we successfully synthesized Mg_2Sn using the mechanical ball milling technique followed by hot pressing, which showed a high carrier mobility of $\sim 90\ cm^2\ V^{-1}\ s^{-1}$ at a high doping concentration ($n \sim 1.8 \times 10^{20}\ cm^{-3}$). A record ZT of 1.4 at 450 °C and a peak power factor (PF) of 55 $\mu W\ cm^{-1}\ K^{-2}$ at 350 °C were obtained in $Mg_2Sn_{0.728}Sb_{0.022}Ge_{0.25}$. The thermoelectric performance of this material surpassed other materials in the temperature range of 50–450 °C in terms of both the efficiency and output power. In this paper, we systematically investigated the alloying effect of Ge in $Mg_2Sn_{1-x-y}Ge_xSb_y$ in terms of the generalized material parameter B^*. It is found that the ZT enhancement due to Ge alloying can be understood as a synergetic effect of an $\sim$25% enhancement in U, $\sim$27% widening in E_g, and $\sim$50% reduction in κ_{lat}. Furthermore, the connection between the material parameter B^* and peak ZT for some classic materials, including $CoSb_3$, Bi_2Te_3 and PbTe, were also discussed.

2. Experimental details

2.1 Synthesis

The synthesis process of $Mg_2Sn_{1-x-y}Ge_xSb_y$ (x = 0–0.3, y = 0–0.025) was similar to our previous work.[35] Elemental powders of Mg, Sn, Ge, and Sb were used for ball milling and then hot pressed at 600–750 °C for 2 minutes.

2.2 Thermoelectric transport properties

The electrical resistivity was measured by a DC-current four-point method, while the Seebeck coefficient was determined by the slope of the voltage difference *versus* temperature difference curve based on a static temperature difference method. The simultaneous measurement of electrical resistivity and Seebeck coefficient was conducted on a commercial system (ZEM-3, ULVAC). The thermal conductivity was calculated from the relationship $\kappa = DC_pd$, where D, C_p, and d are the thermal diffusivity, specific heat, and volumetric density, respectively. The thermal diffusivity was measured by the laser flash method using a commercial system (LFA457, Netzsch). The specific heat capacity was determined using a differential scanning calorimeter (DSC 404 C, Netzsch). The volumetric density was measured by the Archimedes method. The measurement of Hall coefficient, R_H, was carried out on a commercial system (PPMS, Quantum Design), with a magnetic field up to 6 T and an electrical current of 10–20 mA.

2.3 Band gap measurement

Fourier transform infrared (FTIR) spectroscopy is performed to derive the optical band gap based on the Kramers–Kronig analysis of the reflectance. FTIR spectroscopy is conducted on an infrared spectroscopy (iS50, Thermo Nicolet) using a DTGS detector at room temperature in the range of 4000 to 400 cm^{-1} with a resolution of 4 cm^{-1}. The reflectance spectra $R(\omega)$ was taken with an angle of 10° near normal incident direction.

2.4 Theoretical calculation

First principles calculations are performed for the band structures of Mg_2Sn and Mg_2Ge using the linearized augmented plane-wave (LAPW) method[36] as implemented in the WIEN2K simulation package.[37] The generalized gradient approximation (GGA) of Perdew, Burke, and Ernzerhof[38] is used with a Brillouin zone sampling including more than 200 k-points in the irreducible wedge of the Brillouin zone. The newly developed TB-mBJ function[39] is also applied for improving the calculation of the band structure and especially the band gap. Basis sets are determined by $R_{MT}K_{max} = 8$, where R_{MT} is the smallest muffin-tin radius, and K_{max} is the maximum value of reciprocal-lattice vectors. The LAPW sphere radii for Mg, Sn, and Ge are chosen to be $2.2a_0$, where a_0 is the lattice constant determined from the experiment. Besides, the relativistic effects for the valence electrons are included at the scalar relativistic level.

3. Results

Fig. 1 shows the temperature dependent thermoelectric properties of $Mg_2Sn_{1-x-y}Ge_xSb_y$ (x = 0, 0.05, 0.1, 0.15, 0.2, 0.25, and 0.3, y = 0.01, 0.015, and 0.02). All the samples show almost linearly increased electrical resistivity and Seebeck coefficient below 300 °C, demonstrating the behavior of a degenerate semiconductor, as shown in Fig. 1(a and b). The Fermi energy (E_f) calculated from the Seebeck coefficient is 0.031–0.049 eV, equal to $(1.2–1.9)k_BT$ at room temperature, above the bottom of the conduction band, E_c. Above 300 °C, the Seebeck coefficient of $Mg_2Sn_{1-x-y}Ge_xSb_y$ with x = 0 and 0.05 shows saturated characteristics while that with x = 0.25 and 0.30 continues to be linearly temperature dependent. Among the samples, $Mg_2Sn_{0.73}Ge_{0.25}Sb_{0.02}$ shows the highest PF, 45 μW cm^{-1} K^{-2} near room temperature and over 50 μW cm^{-1} K^{-2} in a wide temperature range, as shown in Fig. 1(c). Here, Sb was the electron donor. An approximate linear relationship between the carrier concentration and Sb content was observed in $Mg_2Sn_{1-x-y}Ge_xSb_y$, which indicates ~1 carr. per Sb, as shown in Fig. S1(a and b) (ESI†). It is noted that the free charge transferring from Sb atoms is independent of the Ge content (Fig. S1(c), ESI†). Fig. 1(d) plots the Seebeck coefficient *versus* carrier concentration near room temperature for $Mg_2Sn_{1-x-y}Ge_xSb_y$. For samples with y = 0.01, Seebeck coefficient increases from −116 μV K^{-1} for x = 0 to −141 μV K^{-1} for x = 0.1. Furthermore, for samples with x = 0.1 and y = 0.01, x = 0.15 and y = 0.015, x = 0.2 and y = 0.02, there is only a small change in the Seebeck coefficient while a significant increase in carrier concentration from 1.68 × 10^{20} cm^{-3} (x = 0.1, y = 0.01) to 2.70 × 10^{20} cm^{-3} (x = 0.25, y = 0.02). As the Ge content increases beyond 0.2, a maximum Seebeck and the highest PF were achieved in sample $Mg_2Sn_{1-x-y}Ge_xSb_y$ with x = 0.25 and y = 0.02. The Ge content variation in the carrier effective mass of $Mg_2Sn_{1-x-y}Ge_xSb_y$ implies that the band structure significantly changes with Ge, which will be discussed in the next section. Fig. 1(e) shows a significant decrease in thermal conductivity with increased Ge content in $Mg_2Sn_{1-x-y}Ge_xSb_y$. The corresponding thermal diffusivity and specific heat of $Mg_2Sn_{1-x-y}Ge_xSb_y$ are shown in Fig. S2(a and b) (ESI†). Due to the increased PF and the decreased thermal conductivity, the ZT value is significantly enhanced from 0.6 for x = 0 to around 1.4 for x = 0.25, as shown in Fig. 1(f). The sample with higher Ge content (x = 0.3) shows a slightly lower ZT value due to a lower PF. The reproducibility of samples $Mg_2Sn_{0.75-y}Ge_{0.25}Sb_y$ with two different carrier concentrations of 2.7 × 10^{20} (y = 0.02) and 3.0 × 10^{20} cm^{-3} (y = 0.022) is confirmed by three batches for each composition, as shown in Fig. S3 (ESI†). The room temperature Seebeck coefficient is around −147 μV K^{-1} for the samples with carrier concentration of 2.7 × 10^{20} cm^{-3}, while −137 μV K^{-1} for the samples with a carrier concentration of 3.0 × 10^{20} cm^{-3}. A good reproducibility was achieved for both compositions. The coefficient of variation of thermoelectric transport properties from batch to batch is less than 5%. The average ZTs for both compositions are close to 1.4 at 450 °C.

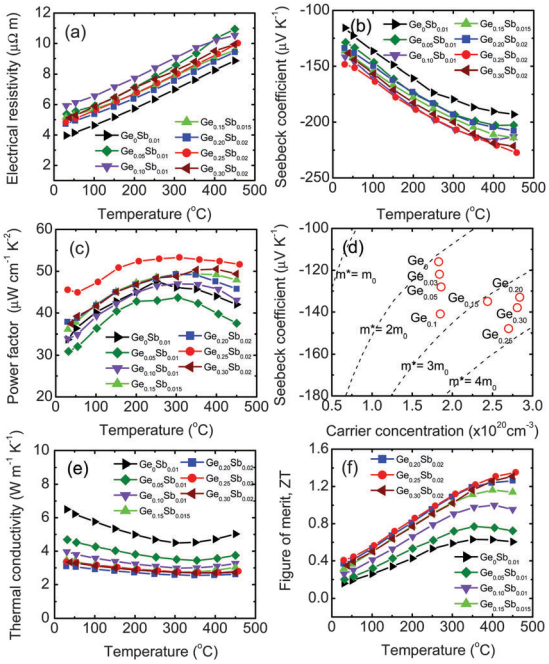

Fig. 1 Thermoelectric properties of $Mg_2Sn_{1-x-y}Ge_xSb_y$. (a) Electrical resistivity, (b) Seebeck coefficient, (c) power factor, (d) Seebeck coefficient *versus* carrier concentration, (e) thermal conductivity, and (f) ZT.

4. Discussion

In the previous section, it is shown how to chemically tune the composition of $Mg_2Sn_{1-x-y}Ge_xSb_y$ to achieve high ZT and PF.

In this section, we will discuss the physical mechanism of the enhanced ZT due to the alloying of Ge in Mg_2Sn. The generalized material parameter B^* will be derived, and the ZT enhancement is then understood in terms of the fundamental parameters U, κ_{lat}, and E_g.

4.1 Generalized material parameter B^*

The original definition of material parameter B was firstly introduced by Chasmar and Stratton through expressing the figure of merit using Fermi–Dirac statistics with non-degenerate approximation as follows,[4,5]

$$ZT = \frac{S^2\sigma T}{\kappa_{lat}+\kappa_{carr}} = \frac{S^2}{\kappa_{lat}/\sigma T + L} = \frac{[(s+5/2)-\xi_f]^2}{[B\exp(\xi_f)]^{-1}+L} \quad (2)$$

$$B = \left(\frac{k_B}{e}\right)^2 \frac{\sigma_0}{\kappa_{lat}} T \quad (3)$$

$$\sigma_0 = 2e\mu\left(\frac{2\pi m^* k_B T}{h^2}\right)^{3/2} \quad (4)$$

where s, L, κ_{lat}, κ_{carr} are the scattering factor, Lorenz number, lattice thermal conductivity, and carrier thermal conductivity, respectively. The definition of s is based on the relaxation time approximation for the electronic transport. For example, $s = -1/2$ for the acoustic phonon dominant scattering case. By using the SI units for the free electron charge (e), free electron mass (m_0), Boltzmann constant (k_B), Plank constant (h), eqn (3) turns into eqn (1). In eqn (2), ZT is only considered as a function of the reduced Fermi level ξ_f, while material parameter B was considered as an independent parameter of ξ_f. A higher B usually corresponds to a higher $(ZT)_{max}$ at optimized ξ_f^*. It is noted that the original definition of B includes variable T, which incorrectly indicates that B increases with temperature T continuously. However, the ZT of a real material drops at high temperatures due to the bipolar effect. To take into account the bipolar effect, it is necessary to use a two band model.[11] For an artificial material with electrons as the major carrier while holes as the minor carrier, eqn (2) can be generalized into the following form (see details in the ESI†),

$$ZT = \frac{\left(\delta_e - \xi_{f\_e} - \frac{\delta_e+\delta_h+\xi_g}{1+1/\gamma}\right)^2 (1+\gamma)}{\left(B\frac{F_{1/2}(\xi_{f\_e})}{\Gamma(3/2)}\right)^{-1} + \frac{(\delta_e+\delta_h+\xi_g)^2}{1+1/\gamma} + L_e + \gamma L_h} \quad (5)$$

for which we have defined

$$\delta_i = \frac{(s+5/2)F_{s+3/2}(\xi_{f\_i})}{(s+3/2)F_{s+1/2}(\xi_{f\_i})}, \quad i = e, h \quad (6)$$

$$L_i = \left(\frac{k_B}{e}\right)^2 \left(\frac{(s+7/2)F_{s+3/2}(\xi_{f\_i})}{(s+3/2)F_{s+1/2}(\xi_{f\_i})} - \left(\frac{(s+5/2)F_{s+3/2}(\xi_{f\_i})}{(s+3/2)F_{s+1/2}(\xi_{f\_i})}\right)^2\right) \quad (7)$$

$$\gamma = \frac{\mu_h (m_h^*)^{3/2}}{\mu_e (m_e^*)^{3/2}} \frac{F_{1/2}(\xi_{f\_e})}{F_{1/2}(\xi_{f\_h})} = \frac{U_h}{U_e} \frac{F_{1/2}(\xi_{f\_e})}{F_{1/2}(\xi_{f\_h})} \quad (8)$$

where $F_n(\xi_f)$ is the nth-order Fermi integral defined as

$$F_n(\xi_f) = \int_0^\infty \frac{\chi^n}{1+e^{\chi-\xi_f}} d\chi \quad (9)$$

and $\xi_g = E_g/k_BT$ is the reduced band gap. The subscript i = e or h represents the electrons and holes, respectively, with the reduced Fermi level ξ_{f_e} (ξ_{f_h}) measured from conduction band edge E_c (valence band edge E_v). According to Simon's early work,[11] ξ_{f_e} and ξ_{f_h} can be described by the reduced Fermi level (ξ_f) of the major carrier band and the reduced band gap ξ_g. For an artificial n-type semiconductor, we have $\xi_{f\_e} = \xi_f$ and $\xi_{f\_h} = -\xi_f - \xi_g$. This relation will be used to replace ξ_{f_e} and ξ_{f_h} hereafter. Furthermore, the ratio U_h/U_e and scattering factor s are considered as constants for convenience in this paper. It is noted that the form of eqn (5) is different from the one Mahan derived, in which a concept of minimum electrical conductivity was adopted.[13] Eqn (5) suggests that the negative impact of the bipolar effect comes from the terms containing ξ_g. If we fix the parameters of B, T, and s, and consider E_g and ξ_f as the tuning variables for ZT, we reproduced Mahan's results: the optimized ZT with respect to ξ_f increases with the band gap and saturates around $E_g \sim 10k_BT$ as shown in Fig. S4 (ESI†). It is noted that the saturated ZT depends not only on material parameter B, but also on U_h/U_e and s.

However, the above analysis has to treat E_g separately from the material parameter B. Here we would like to explore whether we can define a parameter similar to B but including U, κ_{lat}, and E_g altogether, thereby simplifying the evaluation of material's thermoelectric performance. From experimental results, ZT is usually considered as a function of the doping concentration and temperature, *i.e.*, $ZT = f_1(N_D,T)$ for a given set of (U, κ_{lat}, and E_g). In our theoretical formalism, N_D can be described by ξ_f, and hence ZT as a function of ξ_f and T is expressed by eqn (2)–(4) for a single band model with a non-degenerate approximation, and by eqn (5)–(8) for a two band model. Furthermore, we use the reduced band gap $\xi_g = E_g/k_BT$ to non-dimensionalize the temperature, which changes the independent variables of ZT from (ξ_f,T) to (ξ_f,ξ_g), and therefore eqn (5) turns into,

$$ZT = \frac{\left(\delta_e - \xi_f - \frac{\delta_e+\delta_h+\xi_g}{1+1/\gamma}\right)^2 (1+\gamma)}{\left((B^*)\frac{F_{1/2}(\xi_f)/\Gamma(3/2)}{\xi_g}\right)^{-1} + \frac{(\delta_e+\delta_h+\xi_g)^2}{1+1/\gamma} + \left(\frac{e}{k_B}\right)^2 (L_e+\gamma L_h)} \quad (10)$$

with

$$B^* = \frac{1}{k_B}\left(\frac{e}{k_B}\right)^2 \frac{\sigma_{0,e}}{\kappa_{lat}} E_g^{joule} \quad (11)$$

where B^* is defined as the generalized material parameter, and E_g^{joule} is the band energy gap in J as the SI unit. The new definition of the material parameter B^* overcomes the drawback of the conventional definition (eqn (3)) that continuously increases with increasing T. For a given generalized material parameter B^*, ZT can be now considered as a function of the reduced Fermi level and the reduced band gap, *i.e.*, $ZT = f_3(\xi_f, \xi_g)$. Fig. 2 plots the

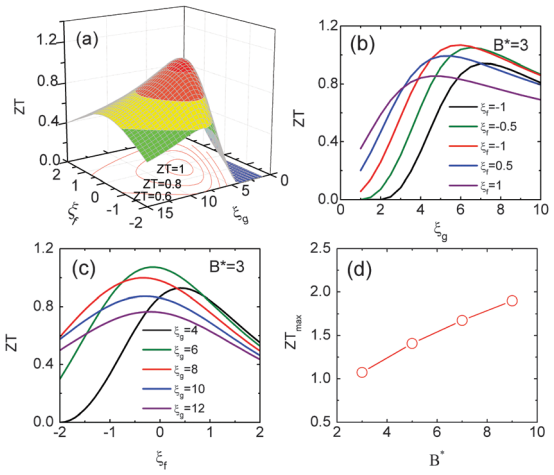

Fig. 2 Theoretical ZT as a function of ξ_f, ξ_g, and B^*. (a) A 3D plot of ZT *versus* ξ_f and ξ_g with a fixed $B^* = 3$, (b) ZT *versus* ξ_g with fixed $B^* = 3$ and $\xi_f = -1, -0.5, 0, 0.5, 1$; (c) ZT *versus* ξ_f with fixed $B^* = 3$ and $\xi_g = 4, 6, 8, 10, 12$; (d) maximum ZT as a function of B^*.

theoretical ZT as a function of ξ_f and ξ_g with assumptions of $s = -1/2$ and $U_e = U_h$. It is clearly shown that ZT has a maximal value with respect to ξ_f and ξ_g for a given generalized material parameter B^*. At $B^* = 3$, the optimized ξ_f and ξ_g for maximizing ZT are close to -0.1 and 6, respectively, as shown in Fig. 2(a). If only ξ_g is considered as the tuning variable, the optimized ξ_g changes from 4 to 7 with ξ_f varying from 1 to -1 as shown in Fig. 2(b). Here, we want to discuss the origin of the qualitative difference in terms of the optimized ZT with respect to the reduced band gap ξ_g between our results (an optimal point) and Mahan's work (saturated behavior). In Mahan's work, the optimized ξ_g is derived by considering E_g as a variable while T is a constant, essentially examining material's properties at a given temperature. In contrast, we optimize ξ_g assuming E_g as a constant while T as the variable, identifying the optimal temperature for a given material. Fig. 2(c) shows ξ_f-dependent ZT for different ξ_g, which suggests that the optimized ξ_f is close to $\xi_f = 0$ and slightly depends on ξ_g. By maximizing ZT with respect to both ξ_f and ξ_g, the final $(ZT)_{max}$ shows a monotonous increase with increasing generalized material parameter B^*, as shown in Fig. 2(d). Combining E_g with U/κ_{lat}, the new material parameter B^* therefore facilitates the search for high-ZT materials over the two-dimensional (doping level and temperature) parameter space. Next, we will consider a simplification of eqn (11). According to the definition of σ_0, the main term are $(m^*)^{3/2}$, μ, and $T^{3/2}$. It is noted that the term of $\mu T^{3/2}$ is a temperature independent parameter for acoustic phonon scattering dominated electron transport since μ depends on $T^{-3/2}$.[9] Therefore, we can define a new temperature-independent parameter U^*, and rewrite the dimensionless material parameter B^* as,

$$B^* = 6.668 \times 10^{-2} \frac{U^*}{\kappa_{lat}} E_g^{eV} \quad (12)$$

$$U^* = \mu (m^*/m_0)^{3/2} T^{3/2} \quad (13)$$

where E_g^{eV} is the band gap in eV as the conventional unit. Furthermore, the expression of B^* clearly suggests that good thermoelectric materials should have higher U^*, larger E_g, and smaller κ_{lat}, which serves as signatures to understand materials' thermoelectric performance and also indicators to rationally guide the search for better thermoelectric materials.

4.2 Enhanced power factor due to increased U^*

Having derived the generalized material parameter B^* in expression of U, κ_{lat}, and E_g as three fundamental parameters that affect ZT, we discuss their changes due to the Ge alloying. Fig. 3 shows thermoelectric transport properties of $Mg_2Sn_{1-x-y}Ge_xSb_y$ as a function of Ge content at room temperature. PF at room temperature of $Mg_2Sn_{1-x-y}Ge_xSb_y$ significantly increased with Ge content from $x = 0.05$ to 0.25, and reached a peak value of 45 μW cm^{-1} K^{-2} at $x = 0.25$, then decreased as the Ge content was further increased to $x = 0.3$, as shown in Fig. 3(a). Hall measurement was conducted to understand the mechanism lying behind. Here, both the Hall coefficient (R_H) and Hall factor (r_H) is used to calculate the real carrier concentration (see details in the ESI†).[32,40]

Considering the real carrier concentration, we split the PF ($S^2\sigma$) into S^2n and μ, as shown in Fig. 3(b and c). Like PF, S^2n increases with Ge content from $x = 0.05$ to 0.25, then decreases. On the other hand, we observed a decrease of μ with increasing Ge in the whole range. In other words, the improved PF, due to the Ge alloying effect, is resulted from the enhanced S^2n which is mainly determined by the effective carrier mass at a given Fermi energy. Fig. 3(d) plots the calculated carrier effective mass of $Mg_2Sn_{1-x-y}Ge_xSb_y$ as a function of the Ge content. Although we have varying content of Sb, m^* of $Mg_2Sn_{1-x-y}Ge_xSb_y$ increases

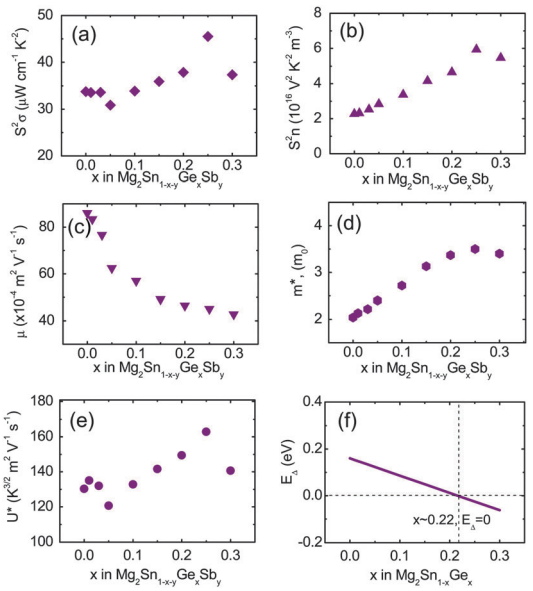

Fig. 3 Effect of Ge content on the thermoelectric properties of $Mg_2Sn_{1-x-y}Ge_xSb_y$. (a) Power factor $S^2\sigma$, (b) S^2n, (c) carrier mobility μ, (d) carrier effective mass m^*, (e) parameter U^*, and (f) the band edge difference between two sub-conduction bands in $Mg_2Sn_{1-x}Ge_x$. (a–f) is the measured data in this study, while the data in (f) are from ref. 28 and 29.

linearly with increasing Ge content from $x = 0$ to 0.2, and reaches a peak value $m^* = 3.5\ m_0$ at $x = 0.25$, and then slightly decreases for the sample with $x = 0.3$. The change of m^* could be understood through the contribution of the additional band above the bottom of the conduction band. Since the significant enhancement of m^*, the parameter U^* (defined in eqn (3)) also appears in similar behavior with Ge content, as shown in Fig. 3(e). Fig. 3(f) shows the composition dependent band structure evaluation in the $Mg_2Sn_{1-x}Ge_x$ system, according to the early work.[28,29] Here, the E_Δ value is the edge difference between two sub-bands in the conduction band. For Mg_2Sn, the additional band is about 0.16 eV higher than the main band. Since $E_\Delta > 5k_BT$, the contribution of the additional band to the total electronic transport is negligible near room temperature.[10] However, E_Δ changes as Ge gets into the Sn-site to form an alloy of $Mg_2Sn_{1-x}Ge_x$. The decreasing E_Δ value with Ge content in the $Mg_2Sn_{1-x}Ge_x$ significantly increases the contribution of the additional band to the electronic transport. Furthermore, a band crossing is predicted around the Ge content of $x = 0.22$ in $Mg_2Sn_{1-x}Ge_x$ according to Zaitsev *et al.*'s work.[28,29] First-principles calculation was conducted to understand the mechanism behind the band convergence between the two sub-bands near the conduction band edge in the Mg_2X (X = Sn, Ge) system. Fig. 4 shows the band structure and total DOS for Mg_2Sn and Mg_2Ge. It is clearly shown that both Mg_2Sn and Mg_2Ge have a valence-band top at the Γ-point and a conduction-band bottom at the X-point, which are consistent with the recently reported calculations.[41,42] Furthermore, two sub-bands at the conduction band edges were observed in both compounds, but the position at the X point was switched. Here, among these two sub-bands at the X-point of Mg_2Sn, the bottom one is referred to as the X_H-band (red color) while the above one is referred to as the X_L-band (blue color). The calculated E_Δ value between the X_H-band and the X_L-band at the X point is around 0.27 eV. The position switching of the X_H-band and the X_L-band at the X-point from Mg_2Sn to Mg_2Ge confirmed the band convergence effect in $Mg_2Sn_{1-x}Ge_x$.[28,29]

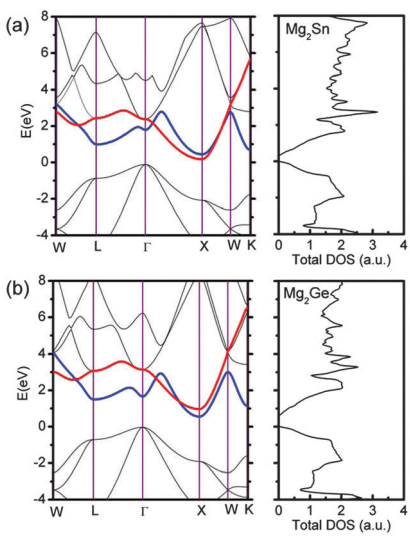

Fig. 4 Band structure and total density of states (DOS) of Mg_2X (X = Sn, Ge). (a) Mg_2Sn, (b) Mg_2Ge. Two sub-conduction band edges were highlighted. The red line denotes the X_H band, while the blue line denotes X_L.

Fig. 5 shows the projected DOS for Mg: s, Mg: p, Sn: s, Sn: p, Sn: d-e_g and Sn: d-t_{2g} orbitals for Mg_2Sn, and Mg: s, Mg: p, Ge: s, Ge: p, Ge: d-e_g and Ge: d-t_{2g} orbitals for the Mg_2Ge. At the first glance, Mg_2Sn has the conduction band mainly composed of unoccupied Mg: 3s orbital (X_H-band) followed by the unoccupied Mg: 3p-Sn: 6s hybridized orbital (X_L-band), while Mg_2Ge has the conduction band mainly consisting of unoccupied Mg: 3p-Ge: 5s hybridized orbital (X_L-band) followed by the Mg: 3s orbital (X_H-band) as shown in Fig. 5(a, b, e and f). In order to get more details, the value of d(p-DOS)/dE *versus* energy was plotted in Fig. 5(c and g) for Mg_2Sn and Mg_2Ge, respectively. We found that the unoccupied Sn: 5d orbital in Mg_2Sn and Ge: 4d orbital in Mg_2Ge are split due to the hexahedral crystalline field into the twice-degenerated d-e_g orbital and triple-degenerated d-t_{2g} orbital. Furthermore, in Mg_2Sn, both the d(p-DOS)/dE of Sn: 5d-t_{2g} and Mg: 3s orbital show a peak at the energy of 0.27 eV, while the d(p-DOS)/dE of Sn: 5d-e_g, Mg: 3p and Sn: 6s shows a peak at an energy of 0.6 eV, as shown in Fig. 5(c and d). Similar coincidence was also observed in Mg_2Ge, as shown in Fig. 5(g and h). These results suggested a new scenario for the conduction band formation of Mg_2Sn and Mg_2Ge. In Mg_2X (X = Sn, Ge), the X_H-band is formed by the hybridized Mg: 3s and Sn: 5d-t_{2g}/Ge:4d-t_{2g} orbitals while the X_L-band results from the hybridized Mg: 3p, Sn: 6s/Ge: 5s, and Sn: 5d-e_g/Ge: 4d-e_g orbitals. The change of the ionic size r^+/r^- ratio could be the most likely reason for the composition band crossing in the $Mg_2Sn_{1-x}Ge_x$ systems. The increased carrier effective mass due to the band crossing is finally responsible for the significant enhancement of the weighted mobility U.

4.3 Decreased bipolar thermal conductivity due to increased E_g

The bipolar effect owing to the intrinsic carrier excitation has a deleterious influence on the thermoelectric performance of materials, which adds a new term in the total thermal conductivity to significantly reduce ZT at high temperature. The thermal conductivity due to the bipolar effect is given by the following relation,[5,11]

$$\kappa_{\text{bipolar}} = \frac{\sigma_e \sigma_h}{\sigma_e + \sigma_h}(S_e - S_h)^2 T \qquad (14)$$

where σ_e, σ_h, S_e, and S_h are the electron conductivity, hole conductivity, electron Seebeck coefficient, and hole Seebeck coefficient, respectively. Conventionally, widening of band gap E_g significantly suppresses the intrinsic excitation, reduces minor carrier, and hence the κ_{bipolar}.

Fig. 6(a and b) shows the estimated bipolar thermal conductivities of $Mg_2Sn_{1-x}Ge_xSb_y$. The detailed numerical calculation about the bipolar thermal conductivity is shown in the ESI.† It is found that adding Ge obviously reduces κ_{bipolar}.

As an example, the bipolar thermal conductivity at 450 °C is 0.2 W m^{-1} K^{-1} for $Mg_2Sn_{0.728}Ge_{0.25}Sb_{0.022}$, but 1.2 W m^{-1} K^{-1} for $Mg_2Sn_{0.99}Sb_{0.01}$. The significant suppression of κ_{bipolar} shifts the peak ZT of $Mg_2Sn_{1-x}Ge_xSb_y$ towards higher temperature. In order to investigate the effect of Ge content on the band gap

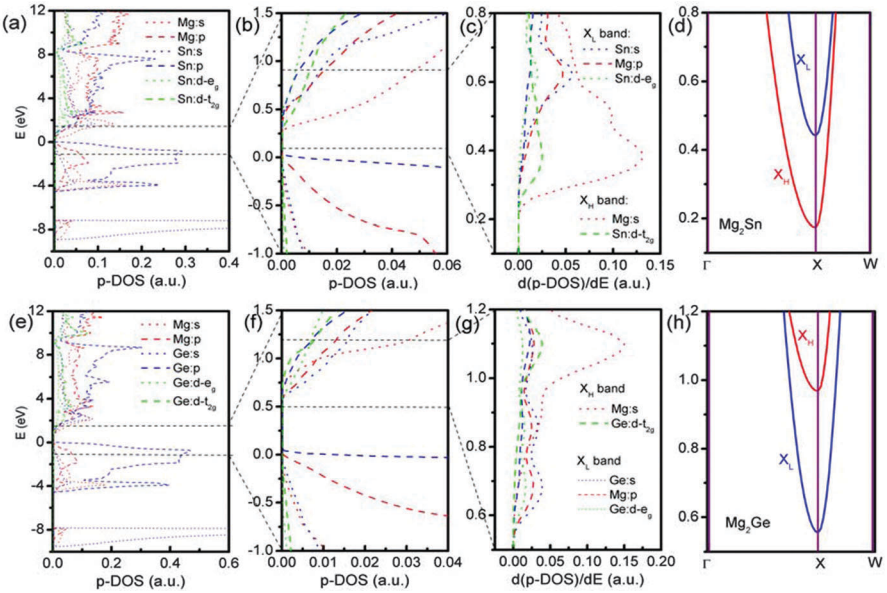

Fig. 5 Projected density of states (DOS) for Mg_2Sn (a–d) and Mg_2Ge (e–h). (a, b, e, and f) Energy *versus* p-DOS; (c and g) energy *versus* d(p-DOS)/dE, (d and h) band structure.

in $Mg_2Sn_{1-x}Ge_xSb_y$, the Fourier transform infrared spectrum of the selected samples were measured to derive the optical band gap. For near-normal incidence, the complex refractive index $n(\omega)$ and the extinction coefficient $k(\omega)$ with both the real and imaginary parts can be obtained from the Kramers–Kronig analysis (see details in the ESI†).[44,45] Fig. 6(c) plots the measured band gap of $Mg_2Sn_{1-x}Ge_xSb_y$ as a function of Ge content. It shows a linear increase from E_g = 0.25 eV to 0.34 eV with increasing Ge content from x = 0 to 0.3. At a given Ge content, our measured band gap is slightly smaller than the values obtained in the early work in $Mg_2Sn_{1-x}Ge_x$,[28,29] which could be due to the heavy doping level of the Sb dopant. Additionally, there is an absorption band in the lower energy range in $Mg_2Sn_{1-x}Ge_xSb_y$ with Ge content $x \geq 0.1$. As an example, such an absorption band is centered at 0.17 eV (Fig. S5, ESI†), which may be related to the electronic transition between multiple conduction bands.[45,46] Furthermore, from our new viewpoint suggested by eqn (10), the widening band gap contributes to the enhancement in the new material parameter B^* and hence an increase of maximum ZT with respect to doping concentration and temperature.

In the case of $Mg_2Sn_{1-x}Ge_xSb_y$, the E_g of $Mg_2Sn_{0.73}Ge_{0.25}Sb_{0.2}$ (E_g = 0.318 eV) is 27% higher than that of $Mg_2Sn_{0.99}Sb_{0.1}$ (E_g = 0.250 eV), which partially contributes to the enhancement in B^* from 0.85 to 2.73, as shown in Table S1 (ESI†). The different B^* values make materials corresponding maximum ZT occur at different optimized doping concentrations and temperatures.

4.4 Decreased lattice thermal conductivity due to the alloying effect

Fig. 7(a and b) show the lattice thermal conductivity (κ_{lat}) dependence on temperature and Ge content in $Mg_2Sn_{1-x-y}Ge_xSb_y$, respectively. Here, the κ_{lat} value was estimated by subtracting the parts contributed by both the charge carriers (κ_{carr}) and $\kappa_{bipolar}$. The details about the numerical calculation were provided in the ESI.† The κ_{lat} at room temperature of $Mg_2Sn_{1-x-y}Ge_xSb_y$ is 4.96, 3.59, 3.10, 2.70, 2.35, 2.33, and 2.27 W m^{-1} K^{-1} for x = 0,

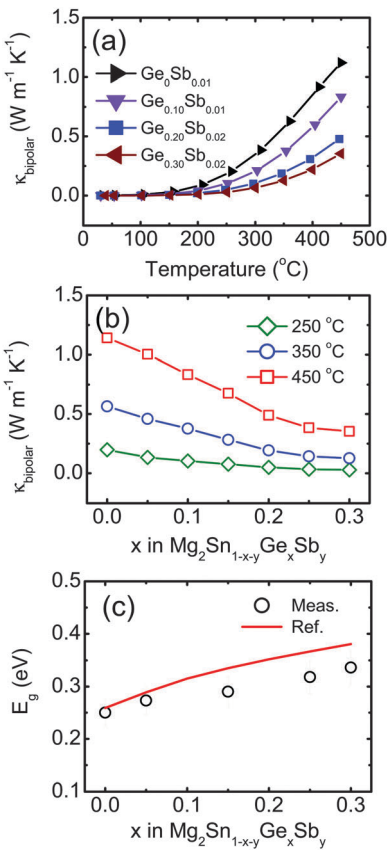

Fig. 6 Calculated bipolar thermal conductivity of $Mg_2Sn_{1-x-y}Ge_xSb_y$ as a function of (a) temperature and (b) Ge content, (c) band gap of $Mg_2Sn_{1-x-y}Ge_xSb_y$ derived from the absorption edge. The reference data in (c) was from ref. 28.

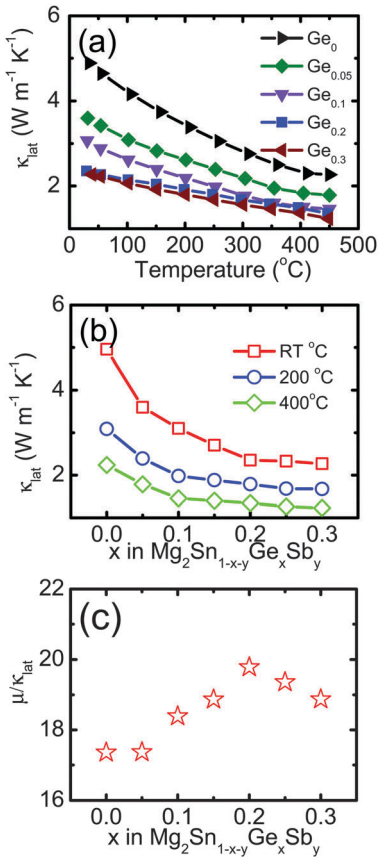

Fig. 7 Calculated lattice thermal conductivity of $Mg_2Sn_{1-x-y}Ge_xSb_y$ as a function of (a) temperature and (b) Ge content, and (c) μ/κ_{lat} of $Mg_2Sn_{1-x-y}Ge_xSb_y$ as a function of Ge content. The unit is $cm^2\ V^{-1}\ s^{-1}$ for μ, $W\ m^{-1}\ K^{-1}$ for κ_{lat}.

0.05, 0.10, 0.15, 0.20, 0.25, and 0.30, respectively. The continuous decrease in κ_{lat} with increasing Ge content demonstrates a strong alloying scattering to phonon transport because of the mass difference between Ge and Sn. It is noted that a similar decrease in μ with increasing Ge was shown before. Fig. 7(c) plots the ratio of μ (unit: $cm^2\ V^{-1}\ s^{-1}$) to κ_{lat} (unit: $W\ m^{-1}\ K^{-1}$) as a function of Ge content in $Mg_2Sn_{1-x-y}Ge_xSb_y$. It shows an increased μ/κ_{lat} ratio with increasing Ge content from $x = 0$ to 0.2, and then a decreased μ/κ_{lat} ratio with $x > 0.2$.

4.5 Relationship between B^* and ZT

With the fundamental parameters U^*, κ_{lat}, and E_g examined, here we show how the ZT enhancement can be understood as a synergistic effect combining all the benefits with regard to the generalized material parameter B^*. Fig. 8(a) plots the peak $(ZT)_{max}$ of $Mg_2Sn_{1-x-y}Ge_xSb_y$ as a function of Ge content. It shows a peak value around the Ge content of $x = 0.25$. In order to explore the connection between ZT and the fundamental parameter B^*, defined in eqn (11), B^* is calculated using U^* and E_g at room temperature and κ_{lat} at temperature corresponding to peak $(ZT)_{max}$, as shown in Fig. 8(b). The calculated B^* shows a continuous increase from 0.85 to 2.73 with increasing Ge content from $x = 0$ to 0.25. Such an enhancement in B^* is contributed by an ~25% enhancement in weighted mobility U^*, ~27% increase in E_g, and ~50% decrease in κ_{lat}. As compared with $x = 0.25$, the sample with Ge of $x = 0.3$ has smaller B^* of 2.56 due to a smaller U^*. The Ge content dependent behavior of B^* is quite similar to that of ZT. Fig. 8(c) plots the peak $(ZT)_{max}$ of $Mg_2Sn_{1-x-y}Ge_xSb_y$ as a function of their corresponding B^*, where it is seen that higher B^* corresponds to a higher $(ZT)_{max}$. In order to further confirm the connection between the $(ZT)_{max}$ and B^*, $(ZT)_{max}$ of selected materials, including $CoSb_3$,[43,47] Bi_2Te_3,[48,49] PbTe[50,51] and FeNbSb[52] was plotted as a function of their estimated B^* in Fig. 8(d). The detailed estimated U^*, E_g, and κ_{lat} are summarized in Table S1 (ESI†). It is noted that the reported $(ZT)_{max}$ could be either lower or higher than theoretical $(ZT)_{max}$ with optimized (ξ_f,ξ_g) (or (N_D,T)) according to eqn (10), because of the limited investigated dopant concentration or the measurement error. A 10% error bar is therefore added in the $(ZT)_{max}$. On the other hand, the estimated B^* could be less accurate since we do not have the measured m^* and μ for U^*, and measured E_g for some of the samples. In this case, the term of $\mu\ (m^*)^{3/2}$ is estimated from the measured σ and S, while E_g is estimated using formula $E_g = 2eS_{max}T$.[53] A 15% error bar is therefore added to B^*. A similar conclusion that a higher B^* leads to a higher $(ZT)_{max}$ is seen in Fig. 8(d). For comparison, the $(ZT)_{max}$ *versus* conventional material parameter B is shown in Fig. 8(e and f). Here, $T = 300$ K was used to estimate the B value according to eqn (1). Fig. 8(e) suggests that the conventional material parameter B was still a good guidance for $Mg_2Sn_{1-x-y}Ge_xSb_y$, but not good enough for other materials. It is therefore reasonable

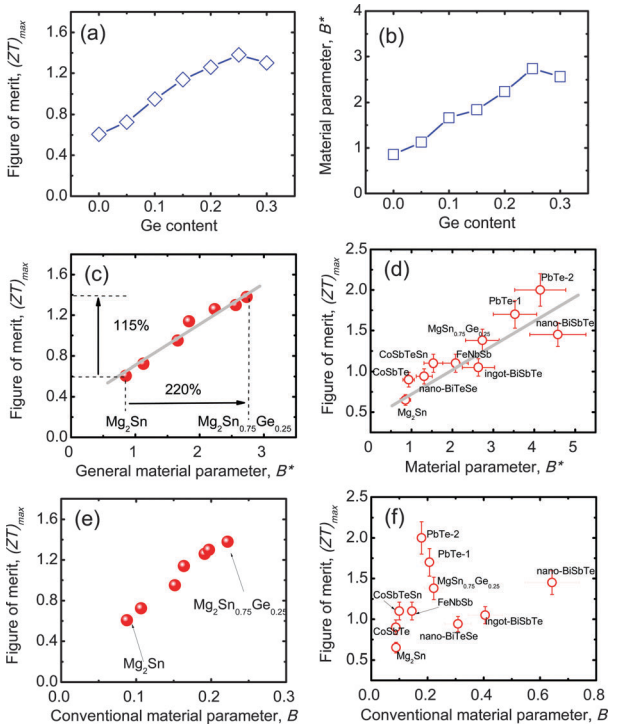

Fig. 8 (a) Ge content dependent peak $(ZT)_{max}$ for $Mg_2Sn_{1-x-y}Ge_xSb_y$, (b) Ge content dependent material parameter B^* for $Mg_2Sn_{1-x-y}Ge_xSb_y$, (c) $(ZT)_{max}$ *versus* B^* for $Mg_2Sn_{1-x-y}Ge_xSb_y$, and (d) $(ZT)_{max}$ *versus* B^* for reported materials. (e) $(ZT)_{max}$ *versus* conventional B for $Mg_2Sn_{1-x-y}Ge_xSb_y$; (f) $(ZT)_{max}$ *versus* conventional B for reported materials.

to consider the generalized material parameter B^* as a new fundamental parameter for exploring better thermoelectric materials, which is directly proportional to U^* and E_g, while inversely proportional to κ_{lat}. Eqn (12) suggests that widening of E_g could have equivalent importance as increased U^* and decreased κ_{lat}. Recently, Zhao *et al.* reported a high ZT_{max} of 2.0 in PbTe with 6%MgTe. One of the favorable effects from MgTe is the suppressed biplolar thermal conductivity due to the widening of the band gap as compared with pure PbTe. The material parameter B^* for PbTe: 6%MgTe was calculated and is included in Fig. 8(d), which also follows the trend. It is noted that the error bar of B^* for PbTe may be even bigger due to the temperature dependent m^* and E_g.[9] In spite of the alloying effect for widening E_g, the carrier filtering effect due to the grain boundary could have a similar band gap widening effect. For example, E_g of nano-BiSbTe (0.184 eV) is slightly larger than that of ingot-BiSbTe (0.167 eV), which is consistent with the reported notable reduction in the bipolar thermal conductivity in nano-BiSbTe.[48] The grain boundary scattering is also responsible for the significant decrease in κ_{lat} from ingot-BiSbTe (0.88 W m^{-1} K^{-1}) to nano-BiSbTe (0.52 W m^{-1} K^{-1}). However, in most cases, the grain boundary has a notorious effect on the carrier mobility, compromising the benefit from the widening band gap and decreased lattice thermal conductivity. A selective scattering mechanism for the carriers is desired for such a kind of carrier filtering grain boundaries. A similar selective carrier filtering effect was noted in half-Heusler materials.[54] As we have pointed out, increasing U^*, reducing κ_{lat}, or widening E_g can be achieved readily. However, it is challenging to synergistically achieve all of them. $Mg_2Sn_{1-x-y}Ge_xSb_y$ is one good example, which shows a simultaneous $\sim$25% enhancement in U^*, $\sim$27% increase in E_g, and $\sim$50% decrease in κ_{lat} by tuning the Ge content, boosting the ZT from 0.6 for $Mg_2Sn_{0.99}Sb_{0.01}$ to 1.4 for $Mg_2Sn_{0.73}Ge_{0.25}Sb_{0.02}$. The new material parameter B^* opens opportunities to further boost the performance of existing materials, and to discover new materials by quantitatively identifying the roles of the fundamental parameters U^*, E_g, and κ_{lat} that affects the thermoelectric performance. It is worth pointing out that the components (U^*, E_g, and κ_{lat}) among the material parameter B^* are still interconnected with each other from more fundamental point of view. In the ESI,† we show a simple discussion about the relationship between U^* and E_g based on $k\cdot p$ perturbation theory,[55] and explain why most thermoelectric materials have a narrow instead of wide band gap. Further explorations into the relation among the parameters in generalized material parameter B^* would be more insightful to guide the researcher to atomically construct ideal materials with optimized atomic sizes, bonding strengths, and crystalline structures.

5. Conclusion

In summary, the significant enhancement in the ZT values of $Mg_2Sn_{1-x-y}Ge_xSb_y$ from 0.6 at x = 0 to 1.4 at x = 0.25 was understood through a generalized material parameter B^*, proposed to be applicable over a wider temperature range, especially taking into account the bipolar effect at high temperatures. This generalized material parameter connects the weighted mobility, lattice thermal conductivity, and the band gap, to characterize material's thermoelectric performance in the two-dimensional (doping level and temperature) parameter space. It is found that the Ge alloying approach leads to an $\sim$25% enhancement in weighted mobility U^*, $\sim$27% increase in E_g, and $\sim$50% decrease in κ_{lat}, which resulted in an $\sim$220% increase in the material parameter B^*. The increased weighted mobility corresponds to a significant enhancement in PF. The band gap widening leads to an appreciable suppression of the bipolar thermal conductivity. $Mg_2Sn_{1-x-y}Ge_xSb_y$ presents a good example to simultaneously tune the three fundamental parameters U^*, κ_{lat}, and E_g. By using the generalized material parameter B^*, the fundamental parameters (U^*, κ_{lat}, and E_g) can be evaluated on the same footing, which we believe will help to better identify new thermoelectric material systems in the future.

Acknowledgements

The authors would like to thank Dr. David, J. Singh at University of Missouri for the helpful advice in the first principles calculation. This work is supported by "Solid State Solar-Thermal Energy Conversion Center (S^3TEC)", an Energy Frontier Research Center funded by the U.S. Department of Energy, Office of Science, Office of Basic Energy Science under award number DE-SC0001299/DE-FG02-09ER46577. Jiming Bao acknowledges support from National Science Foundation (Career Award ECCS-1240510) and the Robert A. Welch Foundation (E-1728)".

References

1 A. F. Ioffe, *Semiconductor thermoelements, and thermoelectric cooling*, Infosearch, London, 1957.
2 C. M. Bhandari and D. M. Rowe, Optimization of carrier concentration, in *CRC handbook of thermoelectric*, ed. D. M. Rowe, CRC Press, Boca Raton, 1995.
3 W. S. Liu, X. Yan, G. Chen and Z. F. Ren, *Nano Energy*, 2012, **1**, 42–56.
4 R. P. Chasmar and R. Stratton, *J. Electron. Control*, 1959, **7**, 52–72.
5 H. J. Goldsmid, *Br. J. Appl. Phys.*, 1960, **11**, 209–217.
6 D. Tuomi, *J. Electrochem. Soc.*, 1984, **131**, 2101–2105.
7 G. D. Mahan, *Solid State Phys.*, 1997, **51**, 81–157.
8 G. S. Nolas, J. Sharp and H. J. Goldsmid, *Thermoelectrics basic principles and new materials developments*, Springer-Verlag, Berlin Heidelberg, 2001.
9 H. Wang, Y. Z. Pei, A. D. LaLonde and G. J. Snyder, Material design considerations based on thermoelectric quality factor, in *Thermoelectric nanomaterials, Springer Series in Materials Science 182*, ed. K. Koumoto and T. Mori, Springer-Verlag, Berlin Heidelberg, 2013, DOI: 10.1007/978-3-642-37537-8_1.
10 W. S. Liu, L. D. Zhao, B. P. Zhang, H. L. Zhang and J. F. Li, *Appl. Phys. Lett.*, 2008, **93**, 042109.

11 R. Simon, *J. Appl. Phys.*, 1962, **33**, 1830–1841.
12 C. Wood, *Rep. Prog. Phys.*, 1988, **51**, 459.
13 G. D. Mahan, *J. Appl. Phys.*, 1989, **65**, 1578–1583.
14 J. O. Sofo and G. D. Mahan, *Phys. Rev. B: Condens. Matter Mater. Phys.*, 1994, **49**, 4565–4570.
15 J. F. Li, W. S. Liu, L. D. Zhao and M. Zhou, *NPG Asia Mater.*, 2010, **2**, 152–158.
16 C. J. Vineis, A. Shakouri, A. Majumdar and M. G. Kanatzidis, *Adv. Mater.*, 2010, **22**, 3970–3980.
17 B. Qiu, Z. T. Tian, A. Vallabhaneni, B. L. Liao, J. M. Mendoza, O. D. Restrepo, X. L. Ruan and G. Chen, *Europhys. Lett.*, 2015, **109**, 57006.
18 M. Zebarjadi, G. Joshi, G. H. Zhu, B. Yu, A. Minnich, Y. C. Lan, X. W. Wang, M. Dresselhaus, Z. F. Ren and G. Chen, *Nano Lett.*, 2011, **11**, 2225–2230.
19 Y. Xiao, G. Joshi, W. S. Liu, Y. C. Lan, H. Wang, S. Y. Lee, J. W. Simonson, S. J. Poon, T. M. Tritt, G. Chen and Z. F. Ren, *Nano Lett.*, 2011, **11**, 556–560.
20 L. D. Zhao, J. Q. He, S. Q. Hao, C. I. Wu, T. P. Hogan, C. Wolverton, V. P. Dravid and M. G. Kanatzidis, *J. Am. Chem. Soc.*, 2012, **134**, 16327–16336.
21 J. P. Heremans, V. Jovovic, E. S. Toberer, A. Saramat, K. Kurosaki, A. Charoenphakdee, S. Yamanaka and G. J. Snyder, *Science*, 2008, **321**, 554–557.
22 Q. Y. Zhang, H. Wang, W. S. Liu, H. Z. Wang, B. Yu, Q. Zhang, Z. T. Tian, G. Ni, S. Y. Lee, K. Esfarjani, G. Chen and Z. F. Ren, *Energy Environ. Sci.*, 2012, **5**, 5246–5251.
23 Q. Zhang, B. L. Liao, Y. C. Lan, K. Lukas, W. S. Liu, K. Esfarjani, C. P. Opeil, D. Broido, G. Chen and Z. F. Ren, *Proc. Natl. Acad. Sci. U. S. A.*, 2013, **110**, 13261–13266.
24 Y. Z. Pei, X. Y. Shi, A. LaLonde, H. Wang, L. D. Chen and G. J. Snyder, *Nature*, 2011, **473**, 66–69.
25 W. Liu, X. J. Tian, K. Yin, H. J. Liu, X. F. Tang, J. Shi, Q. J. Zhang and C. Uher, *Phys. Rev. Lett.*, 2012, **108**, 166601.
26 D. M. Rowe and C. M. Bhandari, *Modern thermoelectrics*, Reston Publishing Company, Reston Virginia, 1983.
27 Z. T. Tian, J. Garg, K. Esfarjani, T. Shiga, J. Shimoni and G. Chen, *Phys. Rev. B: Condens. Matter Mater. Phys.*, 2012, **85**, 184303.
28 V. K. Zaitsev, M. I. Fedorov, I. S. Eremin and E. A. Gurieva, Thermoelectrics on the base of solid solutions of Mg2BIV compounds (BIV = Si, Ge, Sn), in *Thermoelectric handbook: macro to nano structure materials*, CRC Press, New York, 2005.
29 V. K. Zaitsev, M. I. Fedorov, E. A. Gurieva, I. S. Eremin, P. P. Konstantinov, A. Yu. Samunin and M. V. Vedernikov, *Phys. Rev. B: Condens. Matter Mater. Phys.*, 2006, **74**, 045207.
30 R. B. Song, T. Aizawa and J. Q. Sun, *Mater. Sci. Eng., B*, 2006, **136**, 111–117.
31 Q. Zhang, J. He, X. B. Zhao, S. N. Zhang, T. J. Zhu, H. Yin and T. M. Tritt, *J. Phys. D: Appl. Phys.*, 2008, **41**, 185103.
32 X. H. Liu, T. J. Zhu, H. Wang, L. P. Hu, H. H. Xie, G. Y. Jiang, G. J. Snyder and X. B. Zhao, *Adv. Energy Mater.*, 2013, **3**, 1238–1244.
33 A. U. Khan, N. V. Vlachos, E. Hatzikraniotis, G. S. Polymeris, Ch. B. Lioutas, E. C. Stefanaki, K. M. Paraskevopoulos, I. Giapintzakis and Th. Kyratsi, *Acta Mater.*, 2014, **77**, 43–53.
34 L. B. Zhang, P. H. Xiao, L. Shi, G. Henkelman, J. B. Goodenough and J. S. Zhou, *J. Appl. Phys.*, 2015, **117**, 155103.
35 W. S. Liu, H. S. Kim, S. Chen, Q. Jie, B. Lv, M. L. Yao, Z. S. Ren, C. P. Opeil, S. Wilson, C. W. Chu and Z. F. Ren, *Proc. Natl. Acad. Sci. U. S. A.*, 2015, **112**, 3269–3274.
36 D. J. Singh and L. Nordstrom, *Planewaves, pseudopotentials and the LAPW method*, Springer-Verlag, Berlin Heidelberg, 2nd edn, 2006.
37 P. Blaha, K. Sshwarz, G. K. H. Madsen, D. Kvasnicka and J. Luitz, *WIEN2K: an augmented plane wave plus local orbital program for calculating crystal properties*, 2001.
38 J. P. Perdew, K. Burke and M. Ernzerhof, *Phys. Rev. Lett.*, 1996, **77**, 3865–3868.
39 F. Tran and P. Blaha, *Phys. Rev. Lett.*, 2009, **102**, 226401.
40 H. J. Goldsmid, *Applications of Thermoelectricity*, Butler & Tanner, London, 1960.
41 J. J. Pulikkotil, D. J. Singh, S. Auluck, M. Saravanan, D. K. Misra, A. Dhar and R. C. Budhani, *Phys. Rev. B: Condens. Matter Mater. Phys.*, 2012, **86**, 155204.
42 K. Kutorasinski, B. Wiendlocha, J. Tobola and S. Kaprzyk, *Phys. Rev. B: Condens. Matter Mater. Phys.*, 2014, **89**, 115205.
43 W. S. Liu, B. P. Zhang, J. F. Li, H. L. Zhang and L. D. Zhao, *J. Appl. Phys.*, 2007, **102**, 103717.
44 D. M. Roessler, *Br. J. Appl. Phys.*, 1965, **16**, 1119–1123.
45 W. J. Scouler, *Phys. Rev.*, 1969, **178**, 1353–1357.
46 H. G. Lipson and A. Kahan, *Phys. Rev.*, 1964, **133**, A800–A810.
47 W. S. Liu, B. P. Zhang, L. D. Zhao and J. F. Li, *Chem. Mater.*, 2008, **20**, 7526–7531.
48 B. Poudel, Q. Hao, Y. Ma, Y. C. Lan, A. Minnich, B. Yu, X. Yan, D. Z. Wang, A. Muto, D. Vashaee, X. Y. Chen, J. M. Liu, M. S. Dresselhaus, G. Chen and Z. F. Ren, *Science*, 2008, **3420**, 634–638.
49 W. S. Liu, Q. Y. Zhang, Y. C. Lan, S. Chen, X. Yan, Q. Zhang, H. Wang, D. Z. Wang, G. Chen and Z. F. Ren, *Adv. Energy Mater.*, 2011, **1**, 577–587.
50 Q. Y. Zhang, H. Z. Wang, Q. Zhang, W. S. Liu, B. Yu, H. Wang, D. Z. Wang, G. Ni, G. Chen and Z. F. Ren, *Nano Lett.*, 2012, **12**, 2324–2330.
51 L. D. Zhao, H. J. Wu, S. Q. Hao, C. I. Wu, X. Y. Zhou, K. Biswas, J. Q. He, T. P. Hogan, C. Uher, C. Wolverton, V. P. Dravid and M. G. Kanatzidis, *Energy Environ. Sci.*, 2013, **6**, 3346–3355.
52 C. G. Fu, T. J. Zhu, Y. T. Liu, H. H. Xie and X. B. Zhao, *Energy Environ. Sci.*, 2015, **8**, 216–220.
53 H. J. Goldsmid and J. W. Sharp, *J. Electron. Mater.*, 1999, **28**, 869–872.
54 W. S. Liu, Z. F. Ren and G. Chen, Nanostructured thermoelectric materials, in *Thermoelectric Nanomaterials, Springer Series in Materials Science 182*, ed. K. Koumoto and T. Mori, Springer-Verlag, Berlin Heidelberg, 2013, 10.1007/978-3-642-37537-8_1.
55 P. Y. Yu and M. Cardona, *Fundamentals of semiconductors: physics and Materials properties*, Springer-Verlag, Berlin Heidelberg, 2010.